Magnetic Field Enhanced 4-electron Pathway of the Well-aligned Co_3O_4/ECNFs in the Oxygen Reduction Reaction

By: Zheng Zeng, Tian Zhang, Yiyang Liu, Wendi Zhang, Ziyu Yin, Zuowei Ji, and Jianjun Wei

This is the peer reviewed version of the following article:

Z. Zeng, T. Zhang, Y. Liu, W. Zhang, Z. Yin, Z. Ji, J. Wei, Magnetic Field Enhanced 4-electron Pathway of the Well-aligned Co_3O_4/ECNFs in the Oxygen Reduction Reaction, *ChemSusChem.* **2018** 11 (3), 580-588. DOI: 10.1002/cssc.201701947.

which has been published in final form at https://doi.org/10.1002/cssc.201701947. This article may be used for non-commercial purposes in accordance with Wiley Terms and Conditions for Self-Archiving.

Abstract:

The sluggish reaction kinetics of the oxygen reduction reaction (ORR) has been the limiting factor for fuel energy utilization, hence it is desirable to develop high-performance electrocatalysts for a 4-electron pathway ORR. A constant low-current (50 μA) electrodeposition technique is used to realize the formation of a uniform Co_3O_4 film on well-aligned electrospun carbon nanofibers (ECNFs) with a time-dependent growth mechanism. This material also exhibits a new finding of mT magnetic field-induced enhancement of the electron exchange number of the ORR at a glassy carbon electrode modified with the Co_3O_4/ECNFs catalyst. The magnetic susceptibility of the unpaired electrons in Co_3O_4 improves the kinetics and efficiency of electron transfer reactions in the ORR, which shows a 3.92-electron pathway in the presence of a 1.32 mT magnetic field. This research presents a potential revolution of traditional electrocatalysis by simply applying an external magnetic field on metal oxides as a replacement for noble metals to reduce the risk of fuel-cell degradation and maximize the energy output.

Keywords: cobalt | electrocatalysis | carbon nanofibers | electron transfer | magnetic field

Article:

Introduction

Given the promise shown by fuel cells as devices for generating clean and sustainable energy, the desirable electrocatalytic oxygen reduction reaction (ORR) has been widely studied by using steady-state polarization, rotating disk electrodes (RDE), rotating ring-disk electrodes (RRDE), and cyclic voltammetry.[1-3] Electrocatalysts including carbon-based materials, such as glassy carbon (GC), graphite, activated carbon, and carbon nanotubes,[4-7] Pt catalysts (Pt nanoparticles and Pt alloys),[8-10] and transition metal-based catalyst (cobalt and iron) have been reported for conducting the ORR.[11-14] ORR performance varies with synthesis conditions, nitrogen doping, metal type, and pyrolysis temperature.[15-18] To ensure that the fuel cell generates the maximum power output, a 4-electron pathway (from oxygen to water) is necessary because the 2-electron pathway (from oxygen to hydrogen peroxide) involved in the cathodic process seriously

compromises the energy yield of the fuel cell. Moreover, the cell membranes and other supporting materials will be impaired in the presence of excess hydrogen peroxide, owing to peroxide radicals generated from a disproportionation reaction.[19, 20]

With a view to a route to a 4-electron pathway by effectively decomposing generated hydrogen peroxide, catalysis by hematite nanoparticles supported on carbon nanotubes[21] or GC[22] was reported. Although the confinement of oxygen within the catalysts is effective, inhomogeneous surface coverage allows hydrogen peroxide to escape into the bulk solution, which decreases the decomposition efficiency of generated hydrogen peroxide. Furthermore, to ensure that electrochemically generated hydrogen peroxide decomposes to water before it escapes into the bulk solution, the rate of hydrogen peroxide decomposition by catalysts should be faster than the electrochemical generation process. In previous studies, it was found that an external magnetic field over a material with magnetic susceptibility could facilitate the electrochemical reactions, owing to the effects of Lorentz force acting on moving charge/ions, charge density gradient modulation, electron state excitation, and/or oscillatory magnetization.[23, 24] Herein, we propose a new strategy to combine the stable synthesis of a paramagnetic transition metal oxide electrocatalyst and its electron transfer rate enhancement to maximize a 4-electron pathway in the ORR.

The metal oxide Co_3O_4, which incorporates mixed-valence Co^{2+} and Co^{3+}, is known to be one of the most promising electrocatalytic materials for the ORR, with high electrocatalytic activities and ecofriendly properties.[25, 26] Its ORR activity enhancement has been reported by introducing nitrogen doping, oxygen vacancies, hydrogenation, and metal-ion doping,[27, 28] which require additional material replacement or structural modification. Co_3O_4 is itself magnetically susceptibility, owing to its spin/spin–orbit coupling-induced magnetic moment.[29, 30] However, little is known about how an external magnetic field affects the electrochemical performance as an electrocatalyst. In addition, the nitrogen-doped electrospun carbon nanofibers (ECNFs) produced by carbonizing electrospun polyacrylonitrile (PAN) could be an electrocatalyst for the ORR.[31, 32] Aligned ECNF structures may be used as scaffolds to uniformly support metal oxide nanostructures because their alignment could potentially enhance the deposition rate by shortening the distance for electron transport. We hypothesize that the combination of these two materials (Co_3O_4 and well-aligned ECNFs) in a nanoscale structure can improve mechanical properties and electrocatalytic performance for the ORR reaction,[33, 34] and that magnetic susceptibility of unpaired electron spins in Co_3O_4 may play a role in electrocatalysis under a magnetic field. Herein, we describe the design and fabrication of Co_3O_4/ECNFs by wrapping Co_3O_4 onto the well-aligned ECNFs. Furthermore, we explore the magnetic effect on the number of electrons in the ORR pathway at electrodes modified with Co_3O_4/ECNFs (50 μA 5 h electrodeposition) in the presence and absence of mT to sub-mT magnetic fields derived from Helmholtz coils.

Results and Discussion

Co_3O_4 growth characterization and mechanism

The fabrication technique for well-aligned ECNFs is based on a facile electrospinning method with a self-designed sample collector (see the Supporting Information, Figure S1). Different

from a normal cylinder design, four steel poles were welded onto a plate to collect the ECNFs without any substrate. After carbonization, the as-prepared pure ECNFs exhibit a well-aligned structure (Figure 1 a). A nitric acid pretreatment, which introduces hydroxy and carboxyl groups, was used to make the ECNF surface more hydrophilic and to introduce reaction sites for the nucleation of Co_3O_4 crystallites. A constant low current (50 μA) was applied for the electrodeposition by an electrochemical workstation for various times ranging from 1 h to 8 h under an N_2 atmosphere with an aqueous precursor solution containing 20 mm $CoSO_4$ and 100 mm Na_2SO_4. The composites' structures and morphologies were characterized by scanning electron microscopy (SEM; Figure 1 b–h). When the electrodeposition starts, thin films form on the functionalized sites distributed on the fibers (Figure 1 b, c). As electrodeposition continues, the films begin to grow denser/thicker and the fibers are fully covered (Figure 1 d, e). After electrodeposition for 5 h, ECNFs with a nanofiber diameter of about 206 nm are decorated by a Co_3O_4 film with a thickness of about 797 nm, making a total diameter of about 1003 nm (Figure 1 f). Co_3O_4 electrodeposition beyond a 5 h time does not show an obvious thickness increase with the applied constant current (Figure 1 g, h), a feature of self-cessation that probably arises from the increased resistance of the Co_3O_4 layers and low current for electrodeposition.

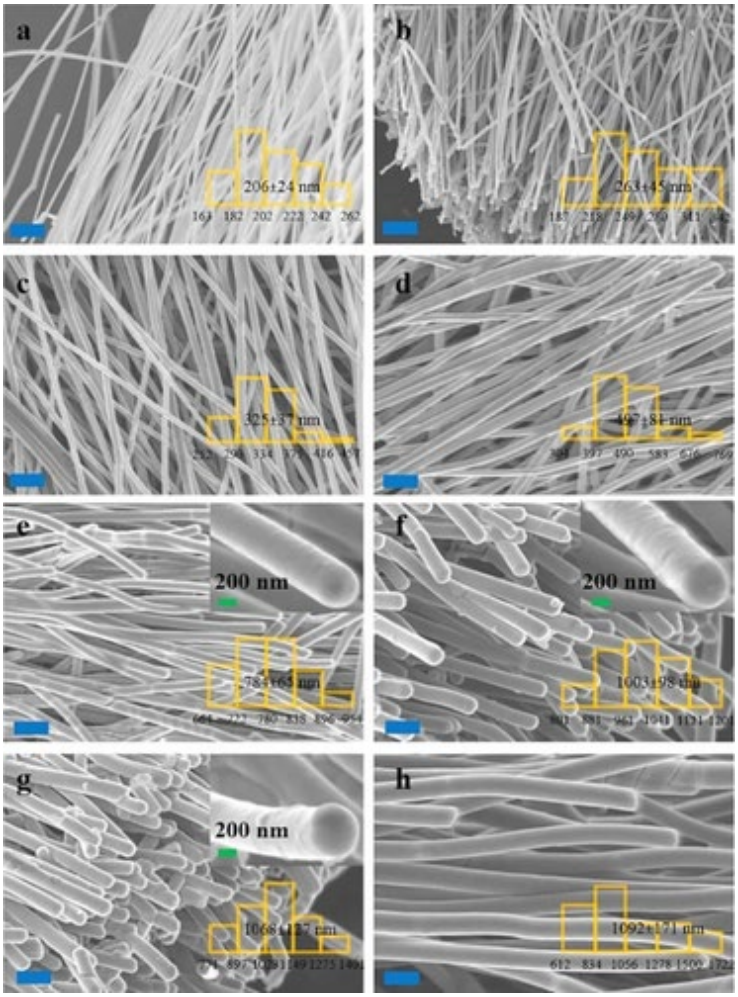

Figure 1. SEM images of well-aligned ECNFs (a) and Co_3O_4/ECNFs for electrodeposition times of 1–8 h (b–h) with the histograms (y axis is the frequency) of size distribution analysis. All of the blue scale bars represent 2 μm.

The chemical composition of the composites under different electrodeposition times from 1 h to 8 h was analyzed by energy-dispersive X-ray (EDX) spectroscopy, Raman spectroscopy, and Fourier transform infrared spectroscopy (FTIR). The EDX spectra (Figure 2 a) show that the surface composition of the electrochemically deposited electrodes is composed of the elements C, O, and Co. The peaks observed at 567 and 668 cm^{-1} in the FTIR spectrum correspond to the stretching vibrations of metal oxide for tetrahedrally coordinated Co^{2+} and octahedrally coordinated Co^{3+} (Figure 2 b),[35] which is further verified by the Raman shifts of 510 and 682 cm^{-1} (Figure 2 c).[36, 37] To investigate the Co_3O_4 crystal structure, the as-prepared Co_3O_4/ECNFs materials were examined by X-ray diffraction (XRD; Figure 2 d; JCPDS No. 009-0418).

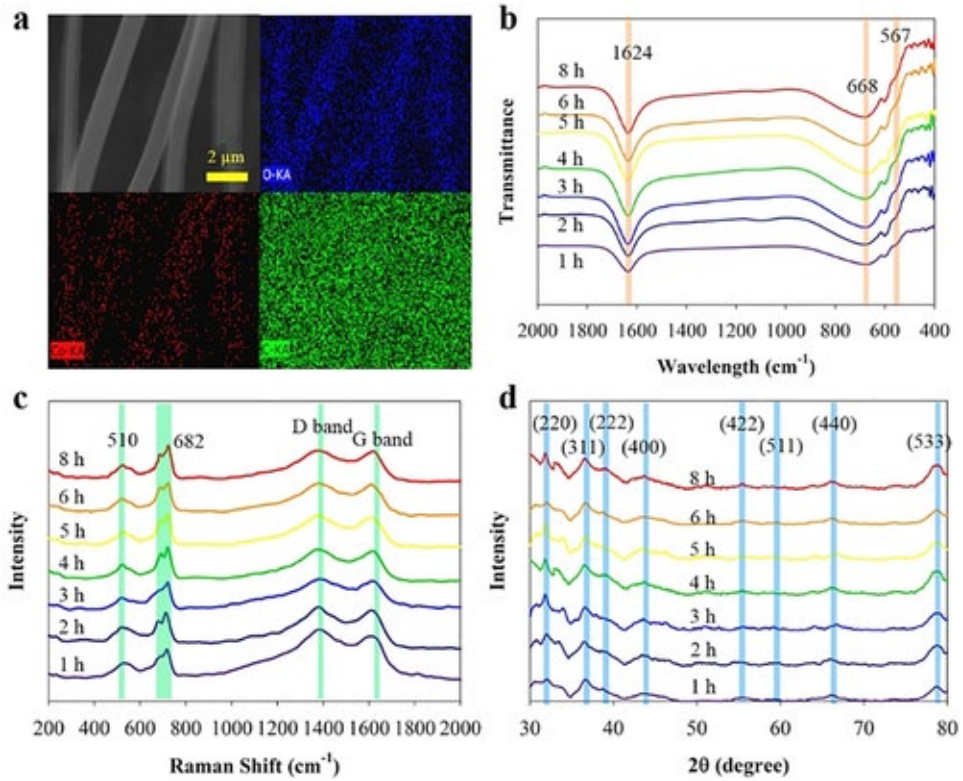

Figure 2. a) SEM associated with EDX mapping analysis of the Co_3O_4/ECNFs under electrodeposition of 5 h. FTIR spectrum (b), Raman spectrum (c), and XRD analysis (d) of the Co_3O_4/ECNFs under electrodeposition times of 1–8 h.

The comprehensive electrodeposition of Co_3O_4 originates from the stable structure of ECNFs, which contributes to a uniform Co^{2+} flux (Figure 3 a). The electrochemical reaction occurs according to Equation 1:

$$3CO^{2+} + 4H_2O \rightarrow CO_3O_4 + 8H^+ + 2e^- \quad (1)$$

In this growth process, the thickness of the Co_3O_4 film can be controlled by the electrodeposition time (Figure 3 b). The growth of the metal oxide film can be analyzed by controlled current electrodeposition kinetics.[38] A general three-step growth model has been derived according to

the measured results, and the Co_3O_4 thickness (h) versus deposition time (t) could be best fit as follows [Equation (2); see the Supporting Information for details]:[39]

$$h = h_{\max}/\left(1 + 10^{(\tau_{0.5} - t)}\right) (t > 0) \quad (2)$$

with $h_{max} \approx 851$ nm and the half-life time constant $\tau_{0.5} \approx 3.59$ h. The time-dependent growth analysis suggests a three-step kinetics mechanism for the electrodeposition (Figure 3 c). The first step involves thin film formation on a boundary layer distributed along the fibers (0–2 h). The second step involves dense film formation and the ECNFs are fully covered (2–5 h). The last step involves the cessation of Co_3O_4 growth and the establishment of a uniform, dense film with a self-limiting thickness (>5 h).

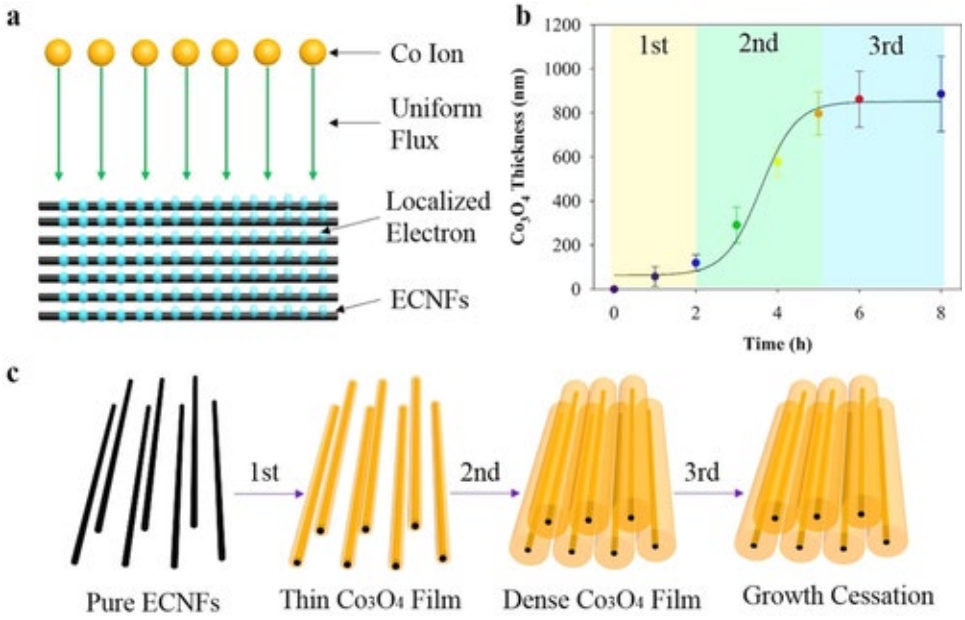

Figure 3. a) Schematic depiction of the Co^{2+} uniform flux. b) Time-dependent Co_3O_4 growth with data analysis. c) Proposed mechanism of Co_3O_4 growth.

Co_3O_4 thickness-dependent electron pathway

The ORR activity was first investigated by studying the cyclic voltammetric responses of a bare GC electrode (Figure S2). The cathodic peak resulted from the electrochemical reduction of oxygen and the magnitude of the cathodic peaks increases with increasing voltage scan rates. The Butler–Volmer model can be used to describe the electrochemical kinetics of the ORR process.[40] In this case, the slope (slope 1) of a plot of log(peak current) versus peak potential (E_p [V]; Figure S3) and Equation (3) are used to determine the transfer coefficient (α):[40]

$$\text{Slope } 1 = \frac{-\alpha F}{2.3RT} \quad (3)$$

where R is the gas constant, F is the Faraday constant, and T is the temperature. In addition, the peak current, i_p [A], is measured as a function of the square root of the voltage scan rate

(v [V s^{-1}]; Figure S4). The slope (slope 2) can be used to characterize the concentration of oxygen in the bulk solution (C [mol mL^{-1}]) through Randles–Sevcik equation:[41,42]

$$|\text{Slope 2}| = (2.99 \times 10^5) n^{3/2} \alpha^{1/2} A C D_0^{1/2} \quad (4)$$

where n is the exchanged electron number during the electrochemical process (n= 2 at a bare GC electrode), A is the active surface area of the bare GC electrode (0.071 cm^2), D_0 is the diffusion coefficient (1.95×10^{-5} cm^2 s^{-1}).[11] When the above constants are applied to an absolute value of slope 2 (obtained from Figure S4), the oxygen concentration of 2.50×10^{-7} mol mL^{-1} can be derived. Changing the range of potential scan rate does not affect the magnitudes of slopes 1 and 2 (Figure S5).

Next the cyclic voltammetric responses of the ORR at the Co_3O_4/ECNFs-modified electrode (1–8 h electrodeposition) were examined to find the number of exchanged electrons. The cyclic voltammograms show an increase in the cathodic peak current (at about −0.5 V) with respect to the scan rate (Figure S6). The cathodic peak presented at about 0.60 V is attributed to the reduction reactions between the Co^{III}/Co^{II} complexes.[43] As mentioned above, Equations (3) and (4) are also used to calculate the number of exchanged electrons in the overall electrochemical processes for electrodes modified with Co_3O_4/ECNFs (1–8 h electrodeposition; for examples, see Figures S7 and S8). The numbers of exchanged electrons were found to be 3.09, 3.27, 3.36, 3.43, 3.48, 3.46, and 3.42 for the Co_3O_4/ECNFs modified electrodes under electrodeposition times of 1, 2, 3, 4, 5, 6, and 8 h, respectively (Table S1). The cyclic voltammogram of a Co_3O_4/ECNFs-modified electrode was also studied in an N_2-saturated 20 mm KCl electrolyte solution containing 1 mm hydrogen peroxide at different scan rates (Figure S9). Because no measurable reduction peak shows for either a bare GC electrode or an ECNFs-modified GC electrode in the same solution (Figure S10), one can conclude that a marked increase in the reduction current at the voltage of the Co_3O_4/ECNFs-modified electrode (−0.5 V vs. Ag/AgCl in Figure S9) results from the electrochemical decomposition of hydrogen peroxide taking place at the electrode surface. It is expected that the hydrogen peroxide molecule generated from the electrochemical reduction of oxygen can be decomposed repeatedly at the surface of a uniform Co_3O_4 film. A 4-electron pathway could be approached with a cycle of oxygen decomposition and regeneration, which is in agreement with the results reported for the ORR catalyzed by hematite nanoparticle-modified electrodes.[22]

Therefore, with the increase of Co_3O_4 thickness (1–5 h electrodeposition), the number of exchanged electrons (n) increases owing to oxygen and hydrogen peroxide are effectively confined within the aligned Co_3O_4/ECNFs system (Figure 4 a). Although there is no obvious thickness difference for Co_3O_4 electrodeposition beyond 5 h in time, it shows a decreased n for Co_3O_4/ECNFs electrodes with 6 h (charge transfer resistance≈137 Ω) and 8 h (charge transfer resistance≈149 Ω) electrodeposition, probably because of the resistance increase. When the electrodeposition time is longer than 5 h, the longer electrodeposition results in a more compact Co_3O_4/ECNFs composite, causing the internal resistance increase, whereas the apparent thickness of the Co_3O_4 film on single ECNF undergoes no obvious change. The resistance was deduced from electrochemical impedance spectroscopy (EIS) Nyquist plots (Figure 4 b) and fitting a Randles circuit model.

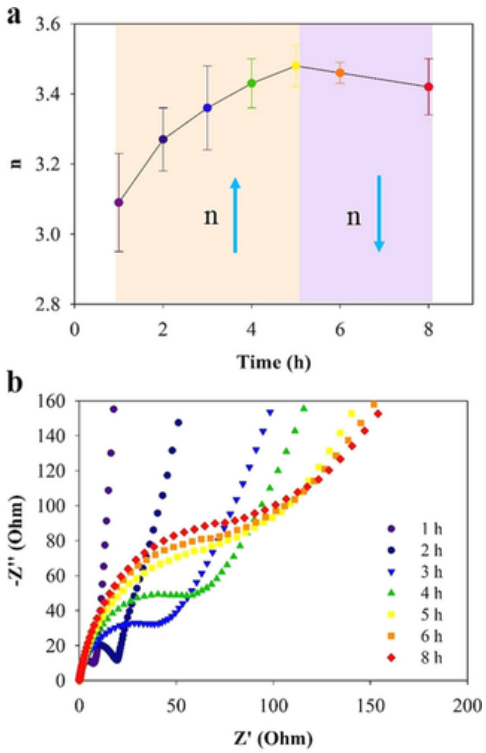

Figure 4. a) Time-dependent exchanged electron number (*n*) of the ORR at the electrode modified with Co_3O_4/ECNFs in O_2-saturated 20 mm KCl electrolyte solution. b) Electrochemical impedance spectroscopy at frequencies from 100 kHz to 0.1 kHz.

Magnetically enhanced electron transfer (MEET)

The cyclic voltammetric responses of the Co_3O_4/ECNFs (5 h electrodeposition) modified electrode for ORR were examined under different magnetic fields (Figure 5 a and Figure S11). According to slope 1 [Eq. (3)] from a plot of log (peak current) versus potential (Figure 5 b) and slope 2 [Eq. (4)] from the peak current position on the square root of the voltage scan rate (Figure 5 c), the increased number of exchanged electrons was obtained for the Co_3O_4/ECNFs-modified electrodes under magnetic fields of 0.22, 0.44, 0.66, 0.88 mT, 1.10 mT, 1.32 mT (Figure 5 d, Table 1). There is no measurable difference in the number of electrons exchanged on the bare GC electrode in absence (Figure S2) or presence (Figure S12) of an external magnetic field at 1.32 mT, suggesting that the external mT-range magnetic field does not have a significant effect on oxygen diffusion/transfer due to the applied magnetic field strength.[44, 45] A small difference in this number was observed for the ECNFs-modified electrode in the absence ($n \approx 2.28$; Figure S13 a) and presence ($n \approx 2.35$, 3.1 % increase; Figure S13 b) of an external magnetic field at 1.32 mT, indicating that the external mT-range magnetic field may promote the transfer of paramagnetic peroxo radicals along the porous structure of the ECNFs as a result of the Lorentz force.[44, 45] However, the hybrid of Co_3O_4 with ECNFs afforded much greater activity (n =3.48 vs. 2.28 at 0 mT). Similar results were reported when Co_3O_4 was supported on graphene[28] or carbon nanotubes.[46] Consequently, the difference (n =3.92 at 1.32 mT vs. 3.48 at 0 mT, corresponding to an increase of 12.6 %) in the number of electrons exchanged in the ORR pathway at the hybrid Co_3O_4/ECNFs-modified electrode is mainly a result of the magnetic field effect on the Co_3O_4 film. Moreover, the magnitude of slope 1 increases with the increase of

magnetic field strength (Table 1), suggesting the occurrence of magnetically enhanced electron transfer (MEET) reactions.[47, 48]

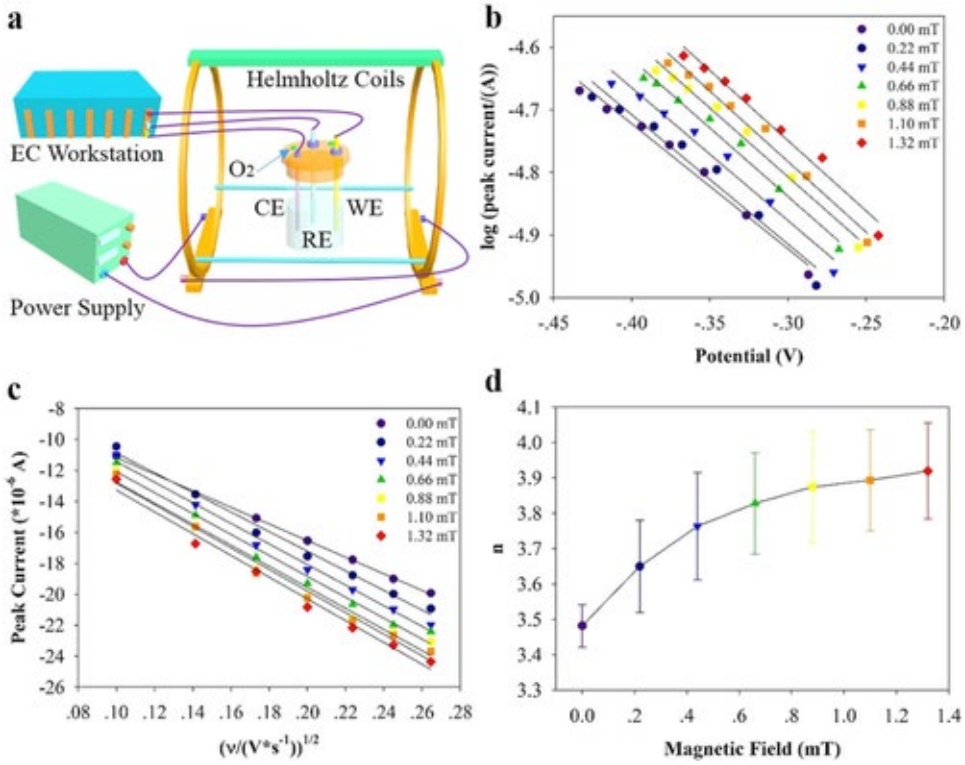

Figure 5. a) Schematic depiction of the magnetic field setup. b) Linear dependence of the log of the peak current on the potential for the transfer coefficient calculation. c) Linear dependence of the peak current on the square root of the scan rate for the exchanged electron number calculation. d) Dependence of the exchanged electron number (*n*) on the magnetic field applied to the ORR at the GC electrode modified with Co_3O_4/ECNFs (5 h electrodeposition).

Table 1. Dependence of the number of exchanged electrons on the magnetic field of the ORR at the electrode modified with Co_3O_4/ECNFs (5 h electrodeposition).

Magnetic field [mT]	**Slope 1**	**Slope 2**	***n***
0.00	−2.10±0.08	$(-5.36\pm0.04)\times10^{-15}$	3.48±0.06
0.22	−2.12±0.14	$(-5.78\pm0.13)\times10^{-5}$	3.65±0.13
0.44	−2.14±0.17	$(-6.08\pm0.14)\times10^{-5}$	3.76±0.15
0.66	−2.19±0.12	$(-6.31\pm0.19)\times10^{-5}$	3.82±0.14
0.88	−2.20±0.11	$(-6.44\pm0.24)\times10^{-5}$	3.87±0.16
1.10	−2.25±0.13	$(-6.56\pm0.18)\times10^{-5}$	3.89±0.14
1.32	−2.28±0.12	$(-6.67\pm0.17)\times10^{-5}$	3.92±0.13

Cyclic voltammetry is a powerful tool to probe the electrochemical kinetics of a redox reaction in solution by an electrode. The heterogeneous rate constant can be derived as a function of the shift in observed reduction peak with the scan rate.[49] The established model was used to estimate the heterogeneous electron-transfer rate constant during the ORR process (k^0_{ORR} [cm s^{-1}]):[49]

$$k_{\mathrm{ORR}}^{0} = 2.18\left(\frac{\alpha D_0 n F v}{RT}\right)\exp\left(\frac{-2\alpha^2 n F\left(E_0 - E_{\mathrm{p}}\right)}{RT}\right) \quad (5)$$

where E_0 is the formal potential determined by the y intercept at a scan rate of 0 mV s^{-1} (Figure 6 a), E_p is the peak potential at scan rate v, and other parameters are the same as mentioned above. By using the experimental results at different scan rates (20 mV s^{-1} in Table S2 as an example) combined with the transfer coefficient, number of electrons exchanged, and diffusion coefficient obtained above, the values of heterogeneous electron transfer rate constant could be calculated (Table S2). With the rate constants obtained under different magnetic fields, a best fit to the experimentally obtained $\ln(k_m/k_0)$ vs. magnetic field (H [T]) gives the following equation (Figure 6 b):

$$\left(\frac{k_{\mathrm{m}}}{k_0}\right)_{\mathrm{ORR}} = \exp(53.99 \cdot H + 0.01) \quad (6)$$

where k_m and k_0 is the electron transfer rate constant of oxygen reduction with and without magnetic fields, respectively.

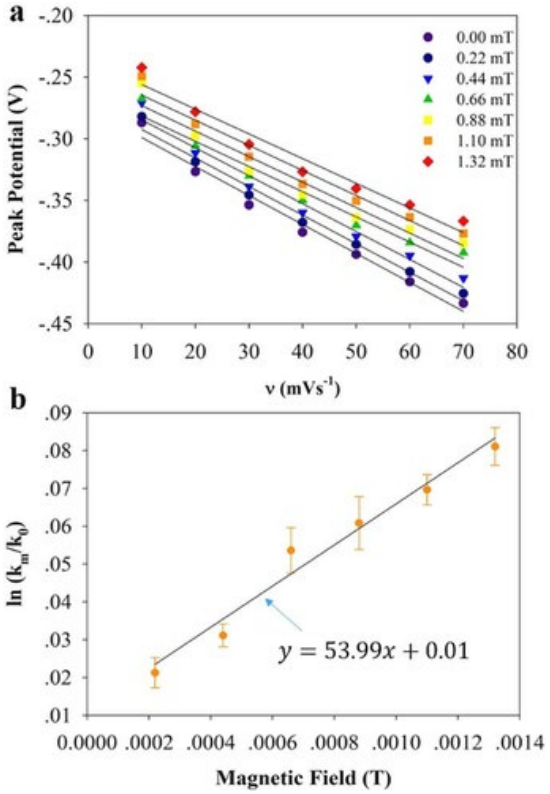

Figure 6. a) Dependence of the peak potential on the scan rate under different magnetic fields of the ORR at the electrode modified with Co_3O_4/ECNFs (5 h electrodeposition). (b) Plot of $\ln(k_m/k_0)$ of oxygen reduction versus magnetic field for the electrode modified with Co_3O_4/ECNFs with linear fit.

Liang et al. reported that the oxygen reduction strongly coupled with cobalt oxide redox reaction.[28] A similar Co^{III}/Co^{II} redox reaction was observed at the Co_3O_4/ECNFs electrode in the presence of oxygen (no redox peaks in the absence of oxygen), suggesting a coupling of the Co^{III}/Co^{II} redox reaction and the ORR process. The magnetic field effect on the electron transfer kinetics of the Co_3O_4 electrode system focusing on the Co^{III}/Co^{II} redox couple (a reduction peak at around 0.5 V vs. Ag/AgCl) at ECNFs was further analyzed by using the Laviron method derived for a diffusionless electrochemical redox reaction system,[50] because the Co^{III}/Co^{II} redox reaction occurs in the deposited Co_3O_4 film. The standard rate constants (k^0) of Co^{III}/Co^{II} were obtained by the fitting of cyclic voltammetry data (Figure 7 a and Figure S14) with the function of overpotential vs. m^{-1}, as expressed by Equation 7:[50]

$$Å_c = mn^{-\gamma}\left\{1 - m(1+\eta)\exp[f(n)]\int_{\infty}^{\eta} x^{-(1+\gamma)}\exp[-f(x)]dx\right\} \quad (7)$$

where $Å_c$ is the function for the cathodic curve, γ is the fitting coefficient, $\eta = \exp[(nF/RT)(E_p - E_0)]$, and $m = (RT/F)(k^0/nv)$. In the absence of an external magnetic field, the standard heterogeneous rate constant for the Co_3O_4/ECNFs electrode system is calculated to be about 0.049 s^{-1}. In the presence of an external magnetic field, the standard rate constants are found to be about 0.063, 0.071, 0.079, 0.086, 0.095, and 0.102 s^{-1} under magnetic fields of 0.22, 0.44, 0.66, 0.88, 1.10, and 1.32 mT (Table S3), respectively.

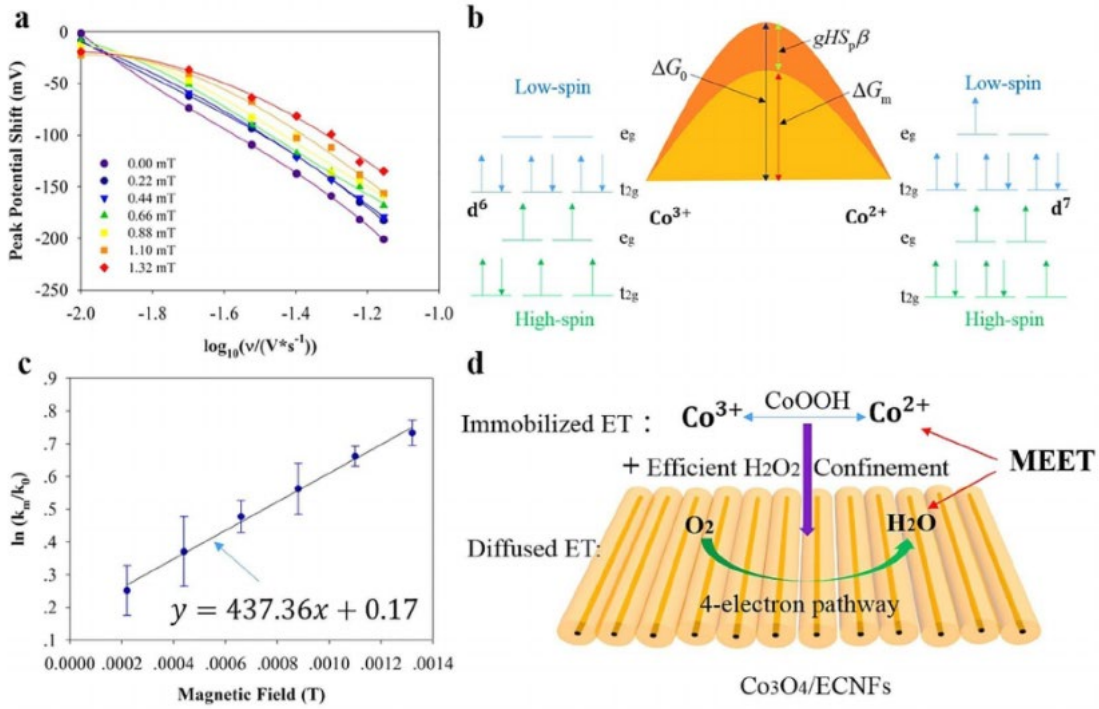

Figure 7. a) Dependence of the peak potential shift on the scan rate under different magnetic fields regarding the electron transfer kinetics of the Co_3O_4 electrode system. b) Schematic depiction of the effects of magnetic field effects on the electronic configuration. c) Plot of $\ln(k_m/k_0)$ versus magnetic field with linear fit regarding the electron transfer kinetics of the Co_3O_4 electrode system. d) Proposed mechanism of the magnetically enhanced 4-electron pathway.

According to transition state theory, magnetic field-induced degeneracy on unpaired electron spins generates enhanced electron energy states that contribute to the activation energy for electron-transfer reactions. Figure 7 b shows schematically the electronic configurations resulting from electron transfer [Co^{3+} ($e_g^0t_{2g}^6$ or $e_g^2t_{2g}^4$) to Co^{2+} ($e_g^1t_{2g}^6$ or $e_g^2t_{2g}^5$)].[51] The increase in Zeeman energy, $g\beta HS_p$,[52] in $Co^{3+/2+}$ in the presence of a magnetic field contributes to the activation energy by reducing the net enthalpy of the activation barrier and thereby facilitating the redox reaction rate.[53] The electron transfer rate constant ratio at the electrode surface can be expressed in Arrhenius form [Equation (8); see the Supporting Information for details]:

$$\frac{k_m}{k_0} = exp\left(\frac{gS_p\beta}{k_BT}\cdot H + \frac{\Delta S_m}{k_B}\right) \quad (8)$$

where g is the magnetic response to an applied magnetic field, S_p is electron spin, β is the Bohr magneton, k_B is Boltzmann's constant, and ΔS_m is the magnetically dependent entropy term. Qualitatively, according to Equation (8), the initial energy is shifted by the Zeeman energy under sufficient magnetic field. Quantitatively, a best fit to the experimentally obtained $\ln(k_m/k_0)$ versus H gives the following equation (Figure 7 c):

$$\left(\frac{k_m}{k_0}\right)_{Co} = \exp(437.36\cdot H + 0.17) \quad (9)$$

According to Equations (6) and (9), the pre-factor (437.36) of MEET for the Co^{III}/Co^{II} redox reaction in the Co_3O_4-electrode system is much larger than that (53.99) for the ORR at the electrode surfaces. To this end, a general summary statement of the data analysis and discussion can be reached: 1) the magnetic field polarization on unpaired electron spin of Co_3O_4 and the energy degeneracy can enhance the kinetics of the Co^{III}/Co^{II} redox reaction (Co^{2+} and Co^{3+} by a CoOOH surface layer[28]) in the Co_3O_4/ECNFs catalytic centers (Figure 7 d); and 2) coupling of the Co^{III}/Co^{II} redox reaction and the ORR process facilitate a faster rate of oxygen reduction by the Co_3O_4/ECNFs to fulfill a nearly 4-electron pathway during the oxygen reduction reaction process:

$$O_2 \xrightarrow{Co_3O_3 \leftrightarrow MEET\,CoOOH} H_2O \quad (10)$$

The ability to generate aligned uniform Co_3O_4 film on nanocarbon substrates for ORR catalysis has been demonstrated as a model system to investigate electrochemical kinetics at the catalyst surfaces. The findings may provide a new perspective on magnetic field effects in ORR electrocatalysis by transition metal oxides.

Conclusions

We have demonstrated a new strategy for uniformly electrodepositing Co_3O_4 on well-aligned ECNFs with a constant low current of 50 μA and have explored the change in mechanism of Co_3O_4 growth with electrodeposition time, which indicated three-stage kinetics of the Co_3O_4 growth process with halfway growth at about 3.59 h. From the Co_3O_4 thickness-

dependent ORR performance, the GC electrode modified with Co_3O_4/ECNFs (5 h electrodeposition) shows a high number of exchanged electrons of 3.48, which is ascribed to the effective confinement of hydrogen peroxide. Furthermore, a significant improvement in exchanged electron number can be achieved by applying an external mT-level magnetic field. This causes magnetic field polarization on the unpaired electron spin of Co_3O_4 and electron energy degeneracy, which facilitates a faster rate of oxygen reduction by the Co_3O_4/ECNFs to fulfill a 4-electron pathway during the oxygen reduction reaction process.

Experimental Section

Fabrication of super-aligned ECNFs

A 10 wt % polyacrylonitrile (PAN; M_w=150 000; Acros Organics) solution in dimethylformamide (Acros Organics) was electrospun onto the collector.[54] The applied positive voltage was 18 kV and the distance between the needle tip and the collector was 15 cm. The collector maintained a rate of 2000 rpm during the electrospinning process to form well-aligned precursors. The obtained sheets were then put into an oxidation and annealing furnace for stabilization to ensure that the fibers did not melt during pyrolysis. The heating rate was 1 °C min^{-1} from room temperature to 280 °C and after which this temperature was maintained for 6 h. The as-stabilized nanofibers were finally carbonized at 1200 °C for 1 h at a heating rate of 5 °C min^{-1} under N_2 atmosphere to yield high mechanical strength ECNFs.

Co_3O_4 electrodeposition on ECNFs

After the well-aligned ECNFs were prepared, Co_3O_4 was electrodeposited onto 1 cm^2 ECNFs with a three-electrode setup with a charging current of 50 μA performed on a bio-logic VMP3 electrochemical workstation. Here, a gold electrode coated with ECNFs, a platinum wire, and Ag/AgCl were used as the working electrode, the counter electrode, and the reference electrode (Fisher Scientific), respectively. To assure that the deposition of Co_3O_4 took place uniformly and firmly at the ECNFs' surfaces, the ECNFs electrode was pretreated with 2 % HNO_3 (J. T. Baker) solution at 60 °C for 2 h to introduce OH and COOH groups to facilitate the deposition. An aqueous precursor solution containing 20 mm $CoSO_4$ (Acros Organics) and 100 mm Na_2SO_4 (Acros Organics) was used as the supporting electrolyte. After deposition, the working electrodes were washed with deionized water and the samples were dried for further experiments.

Characterization

Field-emission scanning electron microscopy (FESEM; Carl Zeiss Auriga-BU FIB FESEM Microscope) was performed to study the morphology of the well-aligned ECNFs and Co_3O_4/ECNFs. Energy-dispersive X-ray spectroscopy (EDX; Hitachi S-4800-I FESEM w. backscattered detector), Raman spectroscopy (Horiba XploRA One Raman Confocal Microscope System), and Fourier transform infrared spectroscopy (FTIR; Varian 670) were employed to study the elemental components of the Co_3O_4/ECNFs. X-ray powder diffraction (XRD; Agilent Technologies Oxford Germini X-Ray Diffractometer) was employed to study the crystal structures of Co_3O_4.

Electrochemical study

Electrochemical performance was performed on a bio-logic VMP3 electrochemical workstation by using a three-electrode testing system with 3 mm diameter GC working electrode, a platinum wire as the counter electrode, and an Ag/AgCl reference electrode (Fisher Scientific) in 20 mm KCl (Sigma–Aldrich) electrolyte solution that was thoroughly degassed with O_2.[22] Note that the neutral chloride solution was deliberately chosen to minimize the dissolution of platinum, since redeposition of platinum occurs on the working electrode in strong acidic or alkaline electrolyte.[55] The electrodeposited square-shape Co_3O_4/ECNFs mat was cut into 3 mm diameter wafers with a thickness of about 80–120 μm and then adhered onto the GC as modified electrodes by using conductive carbon glue (Ted Pella, Inc.) for the electrochemical analysis of oxygen electroreduction.[54] Cyclic voltammetry was then carried out after the modified GC electrode was immersed in a N_2-saturated 20 mm KCl solution for 15 min. Cyclic voltammetry was carried out at different scan rates with a potential window of −1.0 to 0.9 V. The magnetic field setup was conducted by the Helmholtz arrangement of the pair of coils (see the Supporting Information for details).

Acknowledgements
This work was supported by NC state funding through the Joint School of Nanoscience and Nanoengineering (JSNN), a member of the Southeastern Nanotechnology Infrastructure Corridor (SENIC) and the National Nanotechnology Coordinated Infrastructure (NNCI), which is supported by the National Science Foundation (ECCS-1542174).

Conflict of interest
The authors declare no conflict of interest.

Supporting Information
Supporting information is available at https://doi.org/10.1002/cssc.201701947.

References

1. M. Shao, Q. Chang, J. P. Dodelet, R. Chenitz, *Chem. Rev.* 2016, **116**, 3594– 3657.
2. C. Zhu, H. Li, S. Fu, D. Du, Y. Lin, *Chem. Soc. Rev.* 2016, **45**, 517– 531.
3. D. Li, H. Lv, Y. Kang, N. M. Markovic, V. R. Stamenkovic, *Annu. Rev. Chem. Biomol. Eng.* 2016, **7**, 509– 532.
4. B. Erable, D. Féron, A. Bergel, *ChemSusChem* 2012, **5**, 975– 987.
5. K. H. Wu, Q. Zeng, B. Zhang, X. Leng, D. S. Su, I. R. Gentle, D. W. Wang, *ChemSusChem* 2015, **8**, 3331– 3339.
6. A. Anastasopoulos, J. C. Davies, L. Hannah, B. E. Hayden, C. E. Lee, C. Milhano, L. Offin, *ChemSusChem* 2013, **6**, 1973– 1982.
7. K. H. Wu, D. W. Wang, D. S. Su, I. R. Gentle, *ChemSusChem* 2015, **8**, 2772– 2788.
8. S. Guo, D. Li, H. Zhu, S. Zhang, N. M. Markovic, V. R. Stamenkovic, S. Sun, *Angew. Chem. Int. Ed.* 2013, **52**, 3465– 3468; *Angew. Chem.* 2013, **125**, 3549– 3552.
9. S. Moniri, T. Van Cleve, S. Linic, *J. Catal.* 2017, **345**, 1– 10.
10. A. M. Gómez-Marín, J. M. Feliu, *ChemSusChem* 2013, **6**, 1091– 1100.
11. D. Guo, R. Shibuya, C. Akiba, S. Saji, T. Kondo, J. Nakamura, *Science* 2016, **351**, 361– 365.

12. M. Zeng, Y. Liu, F. Zhao, K. Nie, N. Han, X. Wang, Y. Li, *Adv. Funct. Mater.* 2016, **26**, 4397– 4404.
13. D. S. He, D. He, J. Wang, Y. Lin, P. Yin, X. Hong, Y. Li, *J. Am. Chem. Soc.* 2016, **138**, 1494– 1497.
14. J. H. Zagal, M. Koper, *Angew. Chem. Int. Ed.* 2016, **55**, 14510– 14521; *Angew. Chem.* 2016, **128**, 14726– 14738.
15. G. Chen, J. Sunarso, Y. Zhu, J. Yu, Y. Zhong, W. Zhou, Z. Shao, *ChemElectroChem* 2016, **3**, 1760– 1767.
16. S. M. Alia, S. Pylypenko, K. C. Neyerlin, D. A. Cullen, S. S. Kocha, B. S. Pivovar, *ACS Catal.* 2014, **4**, 2680– 2686.
17. H. Shin, H. I. Kim, D. Y. Chung, J. M. Yoo, S. Weon, W. Choi, Y. E. Sung, *ACS Catal.* 2016, **6**, 3914– 3920.
18. T. Sun, Q. Wu, R. Che, Y. Bu, Y. Jiang, Y. Li, Z. Hu, *ACS Catal.* 2015, **5**, 1857– 1862.
19. L. Ghassemzadeh, K. D. Kreuer, J. Maier, K. Muller, *J. Phys. Chem. C* 2010, **114**, 14635– 14645.
20. A. Holewinski, J. C. Idrobo, S. Linic, *Nat. Chem.* 2014, **6**, 828– 834.
21. M. Sun, Y. Dong, G. Zhang, J. Qu, J. Li, *J. Mater. Chem. A* 2014, **2**, 13635– 13640.
22. K. Shimizu, L. Sepunaru, R. G. Compton, *Chem. Sci.* 2016, **7**, 3364– 3369.
23. J. Zhu, M. Chen, H. Qu, Z. Luo, S. Wu, H. A. Colorado, Z. Guo, *Energy Environ. Sci.* 2013, **6**, 194– 204.
24. Z. Zeng, Y. Liu, W. Zhang, H. Chevva, J. Wei, *J. Power Sources* 2017, **358**, 22– 28.
25. Y. Liang, Y. Li, H. Wang, J. Zhou, J. Wang, T. Regier, H. Dai, *Nat. Mater.* 2011, **10**, 780– 786.
26. T. Y. Ma, S. Dai, M. Jaroniec, S. Z. Qiao, *J. Am. Chem. Soc.* 2014, **136**, 13925– 13931.
27. L. Xu, Q. Jiang, Z. Xiao, X. Li, J. Huo, S. Wang, L. Dai, *Angew. Chem. Int. Ed.* 2016, **55**, 5277– 5281; *Angew. Chem.* 2016, **128**, 5363– 5367.
28. Y. Liang, H. Wang, J. Zhou, Y. Li, J. Wang, T. Regier, H. Dai, *J. Am. Chem. Soc.* 2012, **134**, 3517– 3523.
29. P. Dutta, M. S. Seehra, S. Thota, J. Kumar, *J. Phys. Condens. Matter* 2008, **20**, 015218.
30. S. K. Meher, G. R. Rao, *J. Phys. Chem. C* 2011, **115**, 25543– 25556.
31. D. Shin, B. Jeong, B. S. Mun, H. Jeon, H. J. Shin, J. Baik, J. Lee, *J. Phys. Chem. C* 2013, **117**, 11619– 11624.
32. X. Mao, G. C. Rutledge, T. A. Hatton, *Nano Today* 2014, **9**, 405– 432.
33. M. Kim, D. Nam, H. Park, C. Kwon, K. Eom, S. Yoo, J. Jang, H. Kim, E. Cho, H. Kwon, *J. Mater. Chem. A* 2015, **3**, 14284– 14290.
34. C. Alegre, C. Busacca, O. D. Blasi, V. Antonucci, A. S. Arico, A. D. Blasi, V. Baglio, *J. Power Sources* 2017, **364**, 101– 109.
35. V. K. Patel, J. R. Saurav, K. Gangopadhyay, S. Gangopadhyay, S. Bhattacharya, *RSC Adv.* 2015, **5**, 21471– 21479.
36. J. Zhang, W. Gao, M. Dou, F. Wang, J. Liu, Z. Li, J. Ji, *Analyst* 2015, **140**, 1686– 1692.
37. Z. Zeng, W. Zhang, D. M. Arvapalli, B. Bloom, A. Sheardy, T. Mabe, Y. Liu, Z. Ji, H. Chevva, D. H. Waldeck, J. Wei, *Phys. Chem. Chem. Phys.* 2017, **19**, 20101– 20109.
38. K. J. Vetter, *Electrochemical Kinetics: Theoretical Aspects*, Academic Press Inc., New York, 1968.
39. Y. Liu, Z. Zeng, B. Bloom, D. H. Waldeck, J. Wei, *Small* 2017, 1703237.
40. J. Wang, *Analytical Electrochemistry* , 3rd ed., Wiley, Hoboken, 2006.

41. H. Muhammad, I. A. Tahiri, M. Muhammad, Z. Masood, M. A. Versiani, O. Khaliq, M. Hanif, *J. Electroanal. Chem.* 2016, **775**, 157– 162.
42. W. Zhang, Z. Zeng, J. Wei, *J. Phys. Chem. C* 2017, **121**, 18635– 18642.
43. M. Toupin, T. Brousse, D. Bélanger, *Chem. Mater.* 2004, **16**, 3184– 3190.
44. O. Lioubashevski, E. Katz, I. Willner, *J. Phys. Chem. B* 2004, **108**, 5778– 5784.
45. L. Wang, H. Yang, J. Yang, Y. Yang, R. Wang, S. Li, S. Ji, *Ionics* 2016, **22**, 2195– 2202.
46. Y. Liang, H. Wang, P. Diao, W. Chang, G. Hong, Y. Li, M. Gong, L. Xie, J. Zhou, J. Wang, T. Z. Regier, F. Wei, H. Dai, *J. Am. Chem. Soc.* 2012, **134**, 15849– 15857.
47. J. Wei, H. Liu, A. R. Dick, H. Yamamoto, Y. He, D. H. Waldeck, *J. Am. Chem. Soc.* 2002, **124**, 9591– 9599.
48. J. Wei, H. Liu, D. E. Khoshtariya, H. Yamamoto, A. Dick, D. H. Waldeck, *Angew. Chem. Int. Ed.* 2002, **41**, 4700– 4703; *Angew. Chem.* 2002, **114**, 4894– 4897.
49. R. J. Klingler, J. K. Kochi, *J. Phys. Chem.* 1981, **85**, 1731– 1741.
50. E. Laviron, *J. Electroanal. Chem. Interfacial Electrochem.* 1979, **101**, 19– 28.
51. T. Takami, *Functional Cobalt Oxides: Fundamentals, Properties and Applications*, Pan Stanford, Singapore, 2014.
52. S. V. Chapyshev, E. Y. Misochko, A. V. Akimov, V. G. Dorokhov, P. Neuhaus, D. Grote, W. Sander, *J. Org. Chem.* 2009, **74**, 7238– 7244.
53. H. C. Lee, Ph.D. Thesis, University of Iowa (USA), **2010** .
54. Z. Zeng, W. Zhang, Y. Liu, P. Lu, J. Wei, *Electrochim. Acta* 2017, **256**, 232– 240.
55. R. Chen, C. Yang, W. Cai, H. Wang, J. Miao, L. Zhang, S. Chen, B. Liu, *ACS Energy Lett.* 2017, **2**, 1070– 1075.